Pergamon

Int. J. Heat Mass Transfer. Vol. 41, No. 13, pp. 1885–1898, 1998

Printed in Great Britain
0017-9310/98 $19.00+0.00

PII: S0017-9310(97)00353-0

Double-diffusive natural convection in trapezoidal enclosures

J. T. VAN DER EYDEN, TH. H. VAN DER MEER† and K. HANJALIĆ
Section Heat Transfer, Department of Applied Physics, Delft University of Technology, P.O. Box 5046, 2600 GA Delft, The Netherlands

and

E. BIEZEN and J. BRUINING
Dietz Laboratory, Faculty of Earth Sciences, Delft University of Technology, P.O. Box 5028, 2600 GA Delft, The Netherlands

(*Received* 30 *December* 1996 *and in final form* 31 *October* 1997)

Abstract—This paper presents some results of numerical and experimental study of turbulent double-diffusive natural convection of a mixture of two gases in a trapezoidal enclosure with imposed unstable thermal stratification. The geometry and boundary conditions are selected to mimic an idealised situation in underground coal gasification. In the computations turbulent fluxes of momentum, heat and mass were modelled by standard and low-*Re*-number (Launder–Sharma) k–ε eddy diffusivity models with inclusion of thermal and mass buoyancy. The computed mean velocity, temperature and concentration, show satisfactory agreement with measurements, indicating that despite some deficiencies, the numerical model can reproduce most of the essential features of the process.

1. INTRODUCTION

Natural convection flows where the buoyancy forces are a result of both temperature and concentration gradients often occur in nature and in engineering. Examples include double-diffusive convection of heat and pollutants (particularly of dense gases) in atmosphere, of heat and salt in oceans, heat and moisture transport in building structures, heat and material diffusion during solidification and crystal growth, chemical vapour deposition and drying processes, as well as in underground cavities during natural or imposed gasification or burning of coal (see Kuyper *et al.* [1]). In the absence of a significant shear-bearing forced fluid movement the mixing of dissolved species and carrier fluid in such double-diffusive systems is governed by the total density stratification consisting of thermal and concentration contributions. This can be expressed in terms of total density increment $\Delta\rho = \Delta\rho_T + \Delta\rho_\omega = -\rho_0(\beta_T \Delta T + \beta_\omega \Delta\omega)$. Here $\beta_T = -1/\rho_0(\partial\rho/\partial T)_\omega$ and $\beta_\omega = -1/\rho_0(\partial\rho/\partial\omega)_T$ denote the volume expansion coefficients due to unit temperature and concentration changes, respectively. Two stratifications act often opposite with unstable thermal stratification (heating from below) promoting turbulence, while the stable concentration gradient tends to damp turbulent fluctuations. Depending on sign and strength of the thermal and concentration gradients, the mixture can be either fully turbulent, fully laminar, or mixed. In most large-scale processes mentioned the unstable thermal stratification is dominant promoting vigorous turbulence and intensive heat and matter transport. However, despite large bulk Rayleigh or Grashof numbers, transitional or laminar regions may prevail in some regions. Of particular interest are situations when a turbulent mixed layer is trapped by a stable layer above. A separating density interface acts as a mixing barrier, preventing transport from one region of fluid domain into another and impeding the mixing between the turbulent and non turbulent fluids. Such coexistent unstable or stable layers separated by a molecular interface are encountered in atmosphere, oceans and salty lakes, in solar ponds, but also in underground caverns formed due to coal gasification. In technological applications it can be desirable to enhance the process of mixing (e.g. in heavy gas storage and handling), by increasing the unstable stratification (e.g. by heating from below), or to suppress the mixing, e.g. in the case of crystal growth where any instability, transition or even traces of turbulence may cause undesirable crystal inhomogeneities and impurities.

Early studies of double-diffusive natural convection were mainly concerned with phenomena of multi-layer structures separated by sharp density interfaces observed in oceans (e.g. Turner [2], Fernando [3]). A comprehensive early overview of the topic was given by Gebhart and Pera [4]. More recently double-

† Author to whom correspondence should be addressed.

NOMENCLATURE

a	thermal diffusivity [$m^2 s^{-1}$]
B	buoyancy ratio
c_μ, $c_{\varepsilon 1}$, $c_{\varepsilon 2}$, $c_{\varepsilon 3}$	constants in k–ε model
$\mathbb{D}$	diffusion coefficient [$m^2 s^{-1}$]
g_i	gravitational acceleration vector [$m s^{-2}$]
G_k	buoyancy production of turbulent kinetic energy [$m^2 s^{-3}$]
Gr_T	thermal Grashof number
Gr_ω	concentration Grashof number
H	height of enclosure [m]
k	turbulent kinetic energy [$m^2 s^{-2}$]
L	width of enclosure [m]
M	molar mass [kg $mole^{-1}$]
N	molar gas injection rate [mole $m^{-2} s^{-1}$]
Nu	Nusselt number
p	pressure [Pa]
Pr	Prandtl number
P_k	shear production of turbulent kinetic energy [$m^2 s^{-3}$]
Re_t	turbulent Reynolds number
Sc	Scmidt number
Sh	Sherwood number
t	time [s]
T	temperature [K]
T_0	mean reference temperature $=(T_h+T_c)/2$ [K]
u_i	Cartesian velocity components [$m s^{-1}$]
x_i	Cartesian coordinates [m].

Greek symbols

β_T	thermal volumetric expansion coefficient $= -[(1/\rho)(\partial\rho/\partial T)]_0 = 1/T_0$ [K^{-1}]
β_ω	solutal volumetric expansion coefficient $= -[(1/\rho)(\partial\rho/\partial\omega)]_0 = 1/\omega_0+[M_h/(M_l-M_h)]$
ΔT	temperature difference $= T_h-T_c$ [K]
$\Delta\omega$	mass fraction range, $=1$
ε	dissipation rate of turbulent kinetic energy [$m^2 s^{-3}$]
ν	kinematic viscosity [$m^2 s^{-1}$]
ν_t	turbulent viscosity [$m^2 s^{-1}$]
ρ	density [kg m^{-3}]
σ_T	turbulent Prandtl number
σ_ω	turbulent Schmidt number
ω	mass fraction of the heavy gas component
ω_0	mean mass fraction, $=1/2$.

Subscripts

c	cold wall
h	hot wall or heavy gas
l	light gas
n	normal to the wall
t	turbulent or tangent to the wall.

diffusive phenomena related to technological applications are receiving increasing attention and a number of papers reporting on both experimental and numerical investigations can be found in literature, the latter mainly confined to laminar regimes. Numerical studies of the laminar double-diffusive flows in rectangular cavities were reported by Lin *et al.* [5], Béghein *et al.* [6], Nishimura *et al.* [7] and Kamakura *et al.* [8]. Studies of turbulent double-diffusion are more scarce in literature. Modelling of unsteady turbulent double-diffusive systems with density interfaces using a standard high-*Re*-number k–ε model modified to account for thermal and concentration buoyancy, have been reported by Bergman *et al.* [9, 10]. More recently Hanjalić and Musemić [11] discussed different turbulence closure levels for double-diffusive systems and reported a successful computation of several experimentally explored unsteady cases. They used a low-*Re*-number k–ε model with variable turbulent Prandtl–Schmidt numbers derived by algebraic truncation of differential transport equations for turbulent fluxes of heat and species. Kuyper [12] studied turbulent double-diffusive reacting flows in a two-dimensional cavity simulating an underground coal gasification channel. In this study the standard high-*Re*-number k–ε turbulence model was used. All reports mentioned cover only some of the multiple facets of the double-diffusive systems, indicating that modelling of turbulent double-diffusive natural convection is still in an early stage of development.

In the present paper we first discuss possible modelling approaches to the solution of double diffusion in complex situations akin to underground coal gasification. While realizing that more advanced models are needed for accurate predictions of double-diffusive transport, in view of uncertainties encountered in characterising and modelling other phenomena in a real gasification process (complex geometries, chemical reactions, coal characterisation, inaccuracy of experimental data used for model validation, etc.) attention was at present confined to testing the potential of the simple isotropic eddy-diffusivity k–ε model in high- and low-*Re*-number versions, modified to account for both the thermal and concentration buoyancy effects. Results of numerical computations of mean velocity, temperature and concentration fields and of two turbulent stress components in steady and transient regimes will be presented and compared with

experiments for turbulent single (thermal) and double-diffusive natural convection of a binary mixture of gases in a trapezoidal enclosure. Rationale for adopting such a cavity shape and boundary conditions as well as their relation to underground coal gasification can be found in the doctoral thesis of Kuyper [12]. Experimental data, which served for model validation, were obtained in a laboratory model of a cavity with the same shape and boundary conditions. Velocity was measured by Laser Doppler Anemometry (LDA), mean temperature by a Chromel–Alumel thermocouple and mean concentration by a gas-sampling probe connected to a gas chromatograph.

2. MODELLING DOUBLE-DIFFUSIVE NATURAL CONVECTION

The geometry considered has the form of a trapezoid (Fig. 1). The bottom wall of the trapezoid has a constant high temperature, the side walls have a constant low temperature and the top wall is adiabatic. The bottom and side walls both in the experiment and in the simulation were porous. Gases of different densities are injected through these walls simulating the gasification and combustion reactions at the surface of the coal walls. A molar flux of a heavy gas is fixed at the bottom wall and a molar flux of a light gas at the side walls. The top wall is non-reacting and impermeable. The imposed temperature and concentration boundary conditions result in opposing buoyancy forces near the walls. Since gases are injected through the walls, there is a non-zero normal velocity at these walls. The injected gases flow out in the z-direction. The velocity in the z-direction is assumed to be uniform across the x–y plane, and increasing linearly in the z-direction. The z-velocity gradient ($\partial w/\partial z$), which enters the continuity equation follows from an integral mass balance. In this way only the x and y momentum equations have to be solved to calculate the three-dimensional flow.

2.1. *Mathematical formulation*

The mean flow is described by the Reynolds averaged equations of conservation of momentum, energy and mass of each species. The Boussinesq approximation is used, so the density is taken constant except in the buoyancy term where it is linearised in terms of temperature and mass fraction. The resulting equations are

$$\frac{\partial u_i}{\partial x_i} = 0 \tag{1}$$

$$\frac{\partial u_i}{\partial t} + u_j \frac{\partial u_i}{\partial x_j} = -\frac{1}{\rho}\frac{\partial p}{\partial x_i} - [\beta_T (T - T_0) + \beta_\omega (\omega - \omega_0)] g_i + \frac{\partial}{\partial x_j}\left[\nu\left(\frac{\partial u_i}{\partial x_j} + \frac{\partial u_j}{\partial x_i}\right) - \overline{u_i' u_j'}\right] \tag{2}$$

$$\frac{\partial T}{\partial t} + u_i \frac{\partial T}{\partial x_i} = \frac{\partial}{\partial x_i}\left(a \frac{\partial T}{\partial x_i} - \overline{u_i' T'}\right) \tag{3}$$

$$\frac{\partial \omega}{\partial t} + u_i \frac{\partial \omega}{\partial x_i} = \frac{\partial}{\partial x_i}\left(\mathbb{D} \frac{\partial \omega}{\partial x_i} - \overline{u_i' \omega'}\right). \tag{4}$$

The imposed boundary conditions for velocity, temperature and concentration are

bottom wall:

$$u_n = \frac{N_h M_h}{\rho} \quad u_t = 0 \quad T = T_h$$

$$u_n \omega - \mathbb{D} \frac{\partial \omega}{\partial x_n} = \frac{N_h M_h}{\rho} \tag{5a}$$

side walls:

$$u_n = \frac{N_l M_l}{\rho} \quad u_t = 0 \quad T = T_c$$

$$u_n (1 - \omega) + \mathbb{D} \frac{\partial \omega}{\partial x_n} = \frac{N_l M_l}{\rho} \tag{5b}$$

top wall:

$$u_n = 0 \quad u_t = 0 \quad \frac{\partial T}{\partial x_n} = 0 \quad \frac{\partial \omega}{\partial x_n} = 0. \tag{5c}$$

The bottom wall is kept at the hot wall temperature T_h and the molar flux of the heavy gas N_h is fixed. Similarly the side walls are kept at the cold wall temperature T_c and the molar flux of the light gas N_l is fixed. The normal velocity at the walls follows from the fluxes.

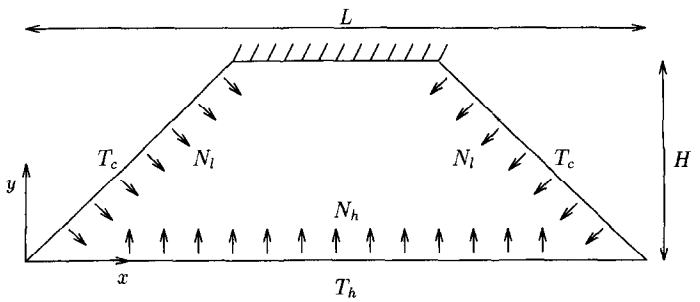

Fig. 1. The trapezoidal cavity with hot and cold walls and injection of a light and heavy gas.

The closure of the equation set (1)–(4) can be achieved in various ways depending on the formulation of turbulent fluxes of momentum, heat and species $\overline{u_i'u_j'}$, $\overline{u_i'T'}$ and $\overline{u_i'\omega'}$, respectively, which constitute a turbulence model. The most advanced approach within the framework of the Reynolds averaging approach will involve modelling and solving the differential transport equation for each flux component ('second-moment closure'), complemented with a transport equation for a characteristic turbulence scale. Such a model contains a large number of empirical coefficients and functions, which for double diffusion problems have not yet been evaluated to a desirable degree of certainty. Besides, a second moment closure poses substantial demands on computation resources which is impractical for computation of complex three-dimensional problems. Nevertheless, second-moment closures may be conveniently truncated to yield simpler models in which turbulent fluxes can be formulated in terms of implicit or explicit algebraic equations (algebraic stress/flux models) which still capture major physical processes. Possible levels of truncations for thermal natural convection have been discussed in more detail by Hanjalić [13] and Dol *et al.* [14] and for double diffusive scalar fields by Hanjalić and Musemić [11]. It will suffice here to recall that a form of algebraic expressions for the turbulent flux of heat and species, containing all important source terms can be written as

$$\overline{u_i'T'} = -C_T\,\overline{u_i'u_j'}\,\frac{\varepsilon}{k}\left[\frac{\partial T}{\partial x_j}+\xi_T\overline{u_j'T'}\,\frac{\partial u_i}{\partial x_j}+\eta_T(\beta_T g_i\overline{T'^2}+\beta_\omega g_i\overline{T'\omega'})\right] \quad (6)$$

$$\overline{u_i'\omega'} = -C_\omega\,\frac{\varepsilon}{k}\left[\overline{u_i'u_j'}\,\frac{\partial\omega}{\partial x_j}+\xi_\omega\overline{u_j'\omega'}\,\frac{\partial u_i}{\partial x_j}+\eta_\omega(\beta_T g_i\overline{T'\omega'}+\beta_\omega g_i\overline{\omega'^2})\right] \quad (7)$$

where ξ and η are coefficients originating from the model of the terms involving fluctuating pressure. Similar expression can be derived for the turbulent stress tensor $\overline{u_i'u_j'}$, which in addition to mean-strain production (almost always positive), contains also the sources due to thermal and concentration buoyancy $\beta_T(g_i\overline{u_j'T'}+g_j\overline{u_i'T'})$ and $\beta_\omega(g_i\overline{u_j'\omega'}+g_j\overline{u_i'\omega'})$. Each of these terms can be either positive or negative, enhancing or damping the turbulent stress field.

Equations (6) and (7), as well as the expression for turbulent stresses (omitted here for brevity) indicate a strong coupling between the two scalar fields and the velocity field. They also illustrate the existence of several sources of turbulent fluxes of momentum, heat and species, which may dominate the transport in various regions of the flow domain. It should be noted for instance, that the turbulent flux of heat and species are only in part governed by the mean temperature/concentration gradients, as implied by the eddy diffusivity hypothesis, but also by the mean velocity gradient and by the scalar field fluctuations themselves associated with buoyancy (terms involving temperature and concentration variances, $\overline{T'^2}$, $\overline{\omega'^2}$) and by buoyant interaction of the two fluctuating scalar fields (correlation $\overline{T'\omega'}$).

While realizing the importance of accounting for various sources of turbulent fluxes, we adopted initially the simplest form of isotropic eddy diffusivity model to check its performance in comparison with available experimental data. Subsequent upgrading of the model was planned by introducing first the anisotropic eddy diffusivity (first term in equations (6) and (7)) and further by incorporating other terms of equations (6) and (7). As shown later, the simple eddy diffusivity model produced acceptable agreement with experiments and, despite some deficiencies, further studies focused on the investigation of the effect of varying boundary conditions in steady and transient regimes, using the same model. A summary of the model equations is outlined below:

$$\overline{u_i'u_j'} = -\nu_t\left(\frac{\partial u_i}{\partial x_j}+\frac{\partial u_j}{\partial x_i}\right)+\frac{2}{3}k\delta_{ij} \quad (8)$$

$$\overline{u_i'T'} = -\frac{\nu_t}{\sigma_T}\frac{\partial T}{\partial x_i} \quad (9)$$

$$\overline{u_i'\omega'} = -\frac{\nu_t}{\sigma_\omega}\frac{\partial\omega}{\partial x_i}. \quad (10)$$

The turbulent Prandtl number σ_T and the turbulent Schmidt number σ_ω are taken constant. The isotropic turbulent viscosity ν_t is defined in standard form in terms of turbulence kinetic energy k and its dissipation rate ε

$$\nu_t = c_\mu\frac{k^2}{\varepsilon}. \quad (11)$$

Two models of transport equations for k and ε were considered. The first model, which we will refer to as the standard k–ε model, uses the high-Re-number form of k and ε transport equations:

$$\frac{\partial k}{\partial t}+u_i\frac{\partial k}{\partial x_i} = \frac{\partial}{\partial x_i}\left(\left(\nu+\frac{\nu_t}{\sigma_k}\right)\frac{\partial k}{\partial x_i}\right)+P_k+G_k-\varepsilon \quad (12)$$

$$\frac{\partial\varepsilon}{\partial t}+u_i\frac{\partial\varepsilon}{\partial x_i} = \frac{\partial}{\partial x_i}\left(\left(\nu+\frac{\nu_t}{\sigma_\varepsilon}\right)\frac{\partial\varepsilon}{\partial x_i}\right)+(c_{\varepsilon1}(P_k+c_{\varepsilon3}G_k)-c_{\varepsilon2}\varepsilon)\frac{\varepsilon}{k} \quad (13)$$

$$P_k = -\overline{u_i'u_j'}\frac{\partial u_i}{\partial x_j} \quad (14)$$

$$G_k = -g_i(\beta_T\overline{u_i'T'}+\beta_\omega\overline{u_i'\omega'}) \quad (15)$$

with standard values of empirical coefficients

$$c_\mu = 0.09 \quad c_{\varepsilon 1} = 1.44 \quad c_{\varepsilon 2} = 1.92 \quad c_{\varepsilon 3} = 1.0$$

$$\sigma_T = 1.0 \quad \sigma_\omega = 1.0 \quad \sigma_k = 1.0 \quad \sigma_\varepsilon = 1.3.$$

This model is only valid for high local turbulent Reynolds number $Re_t = k^2/(\nu\varepsilon)$ and is therefore inapplicable in the viscous region close to a wall. For forced wall-parallel equilibrium flows the problem is usually overcome by use of wall functions, based on the assumption of universal profiles of the flow variables in the near-wall region. These wall functions are inadequate for the flow configuration here considered for several reasons. First, no universal scaling was found for wall-jet type of motion encountered in the near wall region of buoyancy driven flows. Second, we are dealing with permeable walls with fluid injection, which further impedes a universal representation of near-wall profiles of fluid properties. Finally, the geometry considered involves sharp corners (in reality even more complex irregular boundaries), in which the flow is affected by surrounding walls, which is difficult, if not impossible, to represent in a simple functional form valid for a general case. Therefore in conjunction with the high-*Re*-number model we concentrate on its performance away from the walls and ignore near-wall flow behaviour by adopting a simple approach of Henkes [15] where the wall functions are reduced to specifying $k = 0$ and $\varepsilon = \infty$ at the wall.

The second model is the low Reynolds number k–ε model of Launder and Sharma [16, 17], which we will refer to as the Launder–Sharma model. In this model the constants of the standard k–ε model are replaced by functions of the turbulent Reynolds number so that the model is also valid in low turbulence regions,

$$c_\mu = 0.09 \exp\left(-\frac{3.4}{(1+Re_t/50)^2}\right) \tag{16}$$

$$c_{\varepsilon 2} = 1.92(1-0.3\exp(-Re_t^2)). \tag{17}$$

Furthermore the transport equation for ε is replaced by a transport equation for $\tilde{\varepsilon}$ which includes an extra term,

$$\frac{\partial \tilde{\varepsilon}}{\partial t} + u_i \frac{\partial \tilde{\varepsilon}}{\partial x_i} = \frac{\partial}{\partial x_i}\left(\left(\nu + \frac{\nu_t}{\sigma_\varepsilon}\right)\frac{\partial \tilde{\varepsilon}}{\partial x_i}\right)$$

$$+ (c_{\varepsilon 1}(P_k + c_{\varepsilon 3} G_k) - c_{\varepsilon 2}\tilde{\varepsilon})\frac{\tilde{\varepsilon}}{k} + 2\nu\nu_t\left(\frac{\partial^2 u_i}{\partial x_j \partial x_k}\right)^2. \tag{18}$$

$\tilde{\varepsilon}$ is the 'homogeneous' part of ε which, in contrast to ε, is zero at a solid wall, which simplifies the treatment of the wall boundary conditions. The real dissipation rate ε follows from,

$$\varepsilon = \tilde{\varepsilon} + 2\nu\left(\frac{\partial\sqrt{k}}{\partial x_i}\right)^2. \tag{19}$$

The dimensionless parameters that describe the double-diffusive natural convection flow are the thermal Grashof number Gr_T, the concentration Grashof number Gr_ω, the Prandtl number Pr and the Schmidt number Sc,

$$Gr_T = \frac{g\beta_T \Delta T H^3}{\nu^2} \tag{20}$$

$$Gr_\omega = \frac{g\beta_\omega \Delta\omega H^3}{\nu^2} \tag{21}$$

$$Pr = \frac{\nu}{a} \tag{22}$$

$$Sc = \frac{\nu}{\mathbb{D}}. \tag{23}$$

The ratio between mass and thermal buoyancy can be expressed by the buoyancy ratio parameter B,

$$B = \frac{Gr_\omega}{Gr_T}. \tag{24}$$

The ratio between mass and thermal diffusion is defined by the Lewis number Le,

$$Le = \frac{Sc}{Pr}. \tag{25}$$

The local heat transfer rate through a wall can be expressed by the local Nusselt number Nu_x,

$$Nu_x = \frac{u_n T - a\dfrac{\partial T}{\partial x_n}}{a\dfrac{\Delta T}{H}} \tag{26}$$

where u_n is the normal velocity and x_n the normal wall distance. Both convective and diffusive heat transfer are included in the Nusselt number since we will consider walls with non-zero normal velocities. The local mass transfer rates can be expressed similarly by the local Sherwood numbers $Sh_{h,x}$ and $Sh_{l,x}$ for the heavy and light gas, respectively,

$$Sh_{h,x} = \frac{u_n \omega - \mathbb{D}\dfrac{\partial \omega}{\partial x_n}}{\mathbb{D}\dfrac{1}{H}} \tag{27}$$

$$Sh_{l,x} = \frac{u_n(1-\omega) + \mathbb{D}\dfrac{\partial \omega}{\partial x_n}}{\mathbb{D}\dfrac{1}{H}}. \tag{28}$$

In this case the Sherwood number at the wall is fully determined by the molar flux which is fixed at the wall, since $Sh_{h,bot} = (H/(\rho\mathbb{D}))N_h M_h$ and $Sh_{l,side} = (H/(\rho\mathbb{D}))N_l M_l$.

2.2. *Numerical method*

The flow in the trapezium geometry was computed by a finite volume method, using general curvilinear (non-orthogonal) coordinates. The trapezoid was first transformed into a rectangle. The discretized trans-

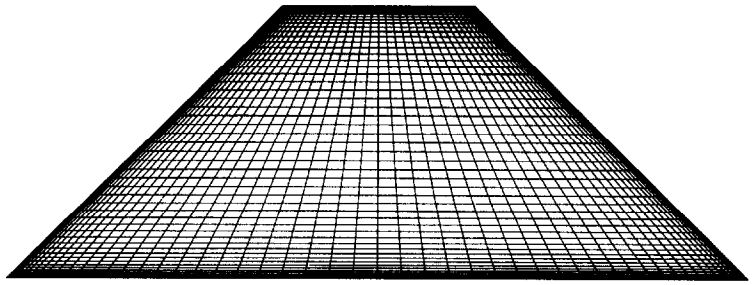

Fig. 2. Computational grid with 60×60 control volumes.

port equations were solved in this rectangle, and afterwards the solution was transformed back to the trapezoid. The transformation method employed enables the flow in arbitrarily shaped geometries to be computed accurately. For a detailed description of this method we refer to Kuyper [18], who used the method to calculate natural convection flows in non-rectangular enclosures. The pressure field and the coupling with the velocity field were resolved using the pressure correction method SIMPLE (Patankar [19]). A non-uniform grid is used, clustered in the vicinity of domain boundaries. Fig. 2 depicts the grid with 60×60 control volumes, used for the standard k–ε model calculations. A finer grid was used for the low-Re-number model, typically with 80×80 control volumes. A grid dependence test with doubling the number of control volumes changed the averaged Nusselt number and the velocity maxima by less than 5%. In view of uncertainty inherent in the turbulence model, the above mentioned grid was adopted as satisfactory and no further refinement was performed. The discretization of the flux through a volume side was performed by using the hybrid scheme. For the time-dependent solution the discrete time step $\Delta t = 0.05$ s was used for flows with a typical period of 20 s. Convergence of the solution was checked by monitoring the change of each variable during iterations and the integrated error in the mass conservation, the velocity, the temperature and the concentration equations. The residual sources were reduced to values smaller than 10^{-6} times a reference value for that criterion.

3. EXPERIMENTAL SET-UP

A schematic view of the trapezoidal cavity used for the experiments is shown in Fig. 1. The height H of the cavity of 0.35 m, the width L 0.96 m and the depth 0.51 m. The side walls make an angle of 45° with the horizontal. The bottom and side walls are made of copper plates, which can be kept at a constant temperature by circulating water or oil. In the plates a large number of small holes is used to inject gases (6700 holes/m^2, hole diameter 0.8 mm). Through the bottom wall argon is injected as heavy gas ($M_{Ar} = 40$ g/mole) and through the side walls nitrogen as light gas ($M_{N_2} = 28$ g/mole). Molar injection rates can be varied in the range 0–0.04 mole/m^2/s. The gases flow out through a blanket in the rear wall. The front wall is made of 5 mm thick poly-carbonate and the top wall of 20 mm thick perspex. All walls are insulated with 20 mm thick poly-urethane foam to minimize heat losses to the surroundings.

To inspect the flow qualitatively, visualization experiments were performed using a laser-sheet. When smoke is injected in the cavity the flow pattern in one plane in the cavity can be observed. Velocity measurements were performed using laser Doppler anemometry (LDA). The mean velocity and the size of the velocity fluctuations in the horizontal and vertical direction are measured (u, v, $\overline{u'^2}$ and $\overline{v'^2}$). The flows studied here have long integral time scales of typically 2 s, therefore the accuracy of the velocity measurements is mainly determined by the averaging time. In this case the variance in the averaged velocity u can be estimated by $2\overline{u'^2}t_{int}/t_{meas}$ [20], where t_{int} is the integral time scale and t_{meas} the averaging time. Substituting typical values ($\overline{u'^2} = 0.002$ m^2/s^2, $t_{int} = 2$ s, $t_{meas} = 180$ s) we obtain an error in the velocity measurements of 7%. The variance of the velocity fluctuations can be estimated similarly by $4\overline{u'^2}^2 t_{int}/t_{meas}$, which gives an error of 20% in the velocity fluctuation measurements. Temperature and concentration measurements were performed using a probe consisting of a thermocouple and a tube to extract gas samples. The probe could be inserted through fittings in the top wall of the cavity. A Chromel–Alumel (type K) thermocouple was used to measure the average temperature locally. The error in the temperature measurement is difficult to estimate due to the different flow conditions and temperature gradients which the thermocouple encounters throughout the cavity. Close to the hot bottom wall, where temperature gradients are largest the temperature measured with the probe differed up to 5°C from the temperature measured with the thermocouples fixed in the wall. This difference can be considered as an upper limit to the error in the temperature measurements. The gas tube of the probe (inner diameter 1.6 mm) is connected to a gas chromatograph (Chrompack CP2002) with a PLOT Molecularsieve 5 Å column, which can measure nitrogen concentration.

Gas samples of approximately 0.5 ml are taken, to enable local concentration measurements. The accuracy of the concentration measurements was found to be below 5% by using a calibration gas. A detailed description of the experimental set-up and the measurements is given by Biezen [21].

4. TEMPERATURE DRIVEN NATURAL CONVECTION

First we present the results of temperature driven natural convection flows in the trapezium. Comparison of calculations and measurements makes it possible to validate the numerical model. The experiments on temperature driven natural convection were performed with air as gas. The temperature of the bottom wall T_h was $57 \pm 3°C$ and the temperature of the side walls T_c was $13 \pm 2°C$. The relevant dimensionless parameters for this configuration are the Prandtl number and the thermal Grashof number. The present computations were performed for air at the reference mean temperature $T_0 = 35°C$ ($\nu = 13.5 \cdot 10^{-6}$ m^2/s, $a = 19.1 \cdot 10^{-6}$ m^2/s, $\rho = 1.292$ kg/m^3) and the height of the cavity $H = 0.35$ m, yielding $Pr = 0.71$ and $Gr_T = 3.4 \cdot 10^8$. The temperature driven flow in the trapezoidal cavity looks similar to the flow in Fig. 6a obtained for a double-diffusive system with a low gas injection rate, which is discussed later.

The velocity field shows that the mean flow consists of a symmetric pattern of two cells. The fluid moves upward in the middle and downward along the cold side walls. The temperature field shows that the temperature is almost uniform over the whole cavity. Large temperature gradients exist only near the bottom and side walls. The turbulent viscosity field shows that turbulence is highest in the top half of the cavity.

A horizontal profile of the horizontal and vertical velocity at $y/H = 0.37$ is shown in Fig. 3. The profiles calculated with the standard k–ε model and the Launder and Sharma model are compared with the experimental data. The differences between the results obtained with two turbulence models are small. The measured velocity profile is not symmetric. This can be attributed to a somewhat non-uniform wall temperature in the measurements. The temperature difference between the right and the left side of the hot bottom wall was approximately 5°C. Calculations using these non-uniform boundary conditions yielded velocity profiles with similar asymmetry.

In general the shape of the calculated profiles agrees well with the measurements. For the horizontal velocity the height of the maxima, both near the walls and near the centre, agree very well. In the vertical velocity profile some deviations between calculation and experiment exist. The height of the central maximum is larger in the calculation than in the experiment. Furthermore the shape of the profile is different, the calculations show a sharp central peak and wide dips at the walls, whereas the measurements

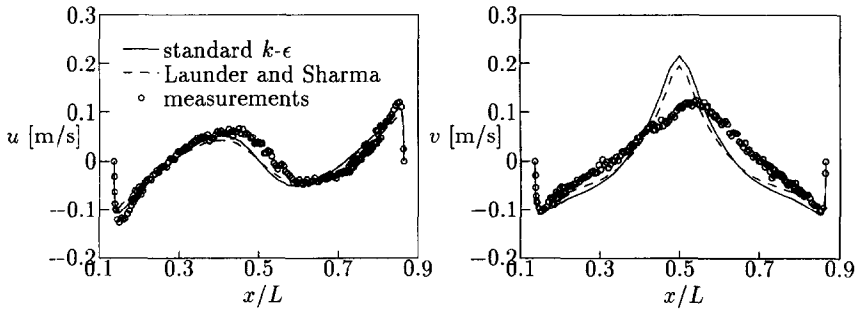

Fig. 3. Horizontal (u) and vertical (u) velocity profiles at $y/H = 0.37$. Lines are simulations, symbols are measurements.

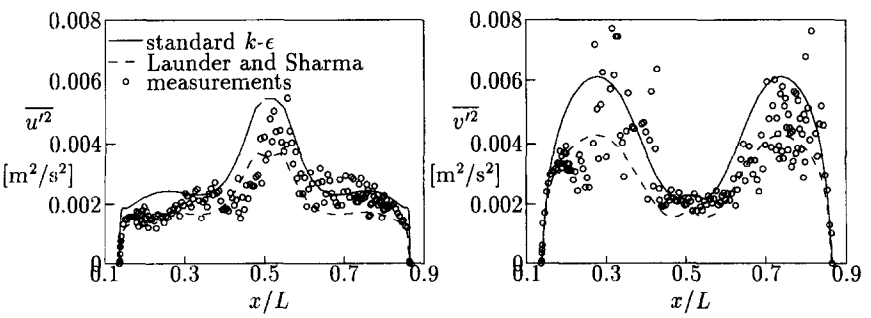

Fig. 4. Horizontal and vertical velocity fluctuation profiles at $y/H = 0.37$. Lines are simulations, symbols are measurements.

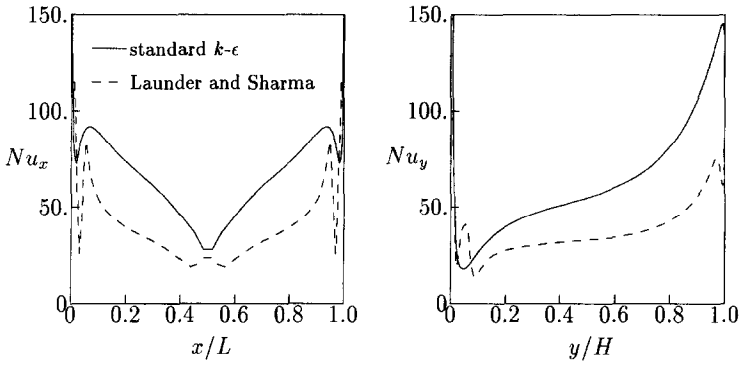

(a) bottom wall (b) side wall

Fig. 5. Calculated local Nusselt number along the hot bottom wall and the cold side wall.

show a wide central peak and sharp dips at the walls. However, the height of the velocity maxima near the wall is predicted well. The vertical velocity maximum is smaller for the Launder and Sharma model than for the standard k–ε model, but still higher than in the measurements.

In the calculated velocity profiles the total upward flow equals the total downward flow since a two-dimensional flow is assumed. This is not the case in the measured profiles. When the measured profiles are integrated we see that about 20% more fluid moves upward then downward. The measurements are made halfway the cavity depth so probably extra fluid moves downward near the front and back wall. This can be a result of heat losses, which make the front and back wall relatively cold and induce a natural convection flow in the z-direction. The discrepancy between the calculated and measured profiles is probably due to these three-dimensional effects.

In Fig. 4 profiles of the velocity fluctuation are shown. The lines are calculated using the eddy-viscosity expression (8) for the two turbulence models and the symbols are results of the LDA measurements. The different turbulence models have significant differences here. The standard k–ε model predicts the highest fluctuation level. With the Launder and Sharma model the shape of the profile is similar but the level is reduced by approximately 25%. The measurements have a large scatter. To reduce this scatter much longer averaging times in the LDA measurements are necessary. However, the profiles still show structure and can be compared with the calculations. The peak in the horizontal velocity fluctuation in the centre and the peaks in the vertical velocity fluctuation with a low plateau in the middle are predicted well. The level of the fluctuations predicted by the standard k–ε model seems somewhat too large. The Launder and Sharma model gives a slightly too low level.

The averaged Nusselt number predicted by the standard k–ε model is $\overline{Nu} = 69.1$, the Launder–Sharma model gives $Nu = 43.2$. The local Nusselt number along the bottom and side wall is shown in Fig. 5. From the corner to the middle along the bottom wall the heat flux decreases and from the bottom to the top along the side wall the heat flux increases. This can be explained by looking at the flow in the cavity. The circulating flow transports hot fluid from the bottom wall via the middle up to the top of the cold side wall, where the heat flux will be high. From the top of the cold side wall the fluid moves downward, the fluid temperature decreases and therefore the heat flux decreases. When the cold fluid reaches the hot bottom wall the heat flux is large. From the corner to the middle the heat flux decreases again due to the increasing temperature of the fluid.

5. DOUBLE-DIFFUSIVE NATURAL CONVECTION

In this section we present the results of the calculations and measurements of double-diffusive natural convection flows. Argon and nitrogen were used as gases in the experiments. Argon was injected through the bottom wall and nitrogen through the side walls. The molar flux of the two gases was always equal, $N_h = N_l = N$. The injection rate N was varied in the range 0–0.04 mol/m^2/s. The temperature settings were the same as for the temperature convection experiments. The bottom wall temperature T_h was 57 ± 3°C and the side wall temperature T_c was 13 ± 2°C.

The relevant dimensionless parameters for this configuration are the Prandtl number, the Schmidt number, the thermal and concentration Grashof number, and the heavy and light gas Sherwood numbers. If we use the properties of a mixture of equal amounts of argon and nitrogen at the mean temperature ($\nu = 15.4 \cdot 10^{-6}$ m^2/s, $a = 22.6$ 10^{-6} m^2/s, $\mathbb{D} = 19.4 \cdot 10^{-6}$ m^2/s, $\rho = 1.292$ kg/m^3), the resulting dimensionless parameters are: $Pr = 0.68$, $Sc = 0.79$, $Gr_T = 2.6 \cdot 10^8$, $Gr_\omega = 6.4 \cdot 10^8$. The buoyancy ratio $B = Gr_\omega/Gr_T = 2.5$ and the Lewis number $Le = 1.16$. The Sherwood numbers for the heavy and light gas injection depend on the injection rate. The heavy gas

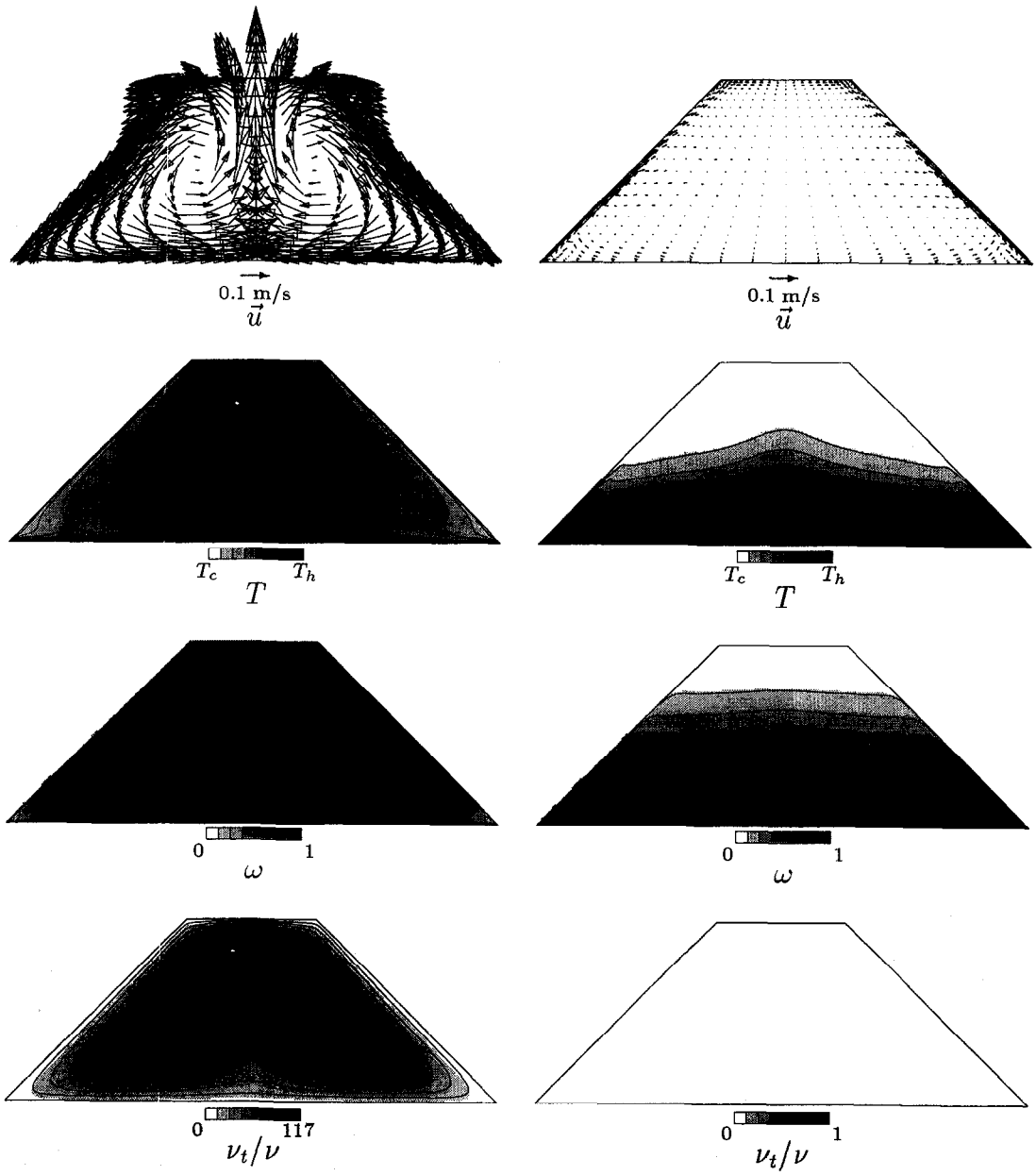

(a) $N = 0.01$ mole/m^{2}s (b) $N = 0.08$ mole/m^{2}s

Fig. 6. Flow in the trapezium for low and high gas injection rate calculated using the standard k–ε model.

Sherwood number Sh_h, representing the argon mass transfer, will be in the range 0–56. The light gas Sherwood number Sh_l, representing the nitrogen mass transfer, will be in the range 0–40 for molar injection rates in the range $N = 0$–0.1 mole/m^2/s.

From the buoyancy ratio $B = 2.5$ we would expect that mass buoyancy is dominant. The concentration Grashof number however is based on a concentration difference from pure argon at the bottom wall and pure nitrogen at the side walls. The concentration is not fixed at the wall in our case. For high injection rates the concentration will be almost pure argon or nitrogen at the walls. For low injection rates the other species will diffuse back to the wall and the concentration difference between the walls will be smaller. Therefore we can still have temperature dominated flow for low injection rates.

5.1. *Flow for different gas injections rates*

In Fig. 6 the flow in the trapezoid calculated using the standard k–ε model is shown for a low and high gas injection rate. For the low injection rate the flow

is similar to the temperature-driven case. The gas moves up in the centre and down along the walls. The concentration field looks similar to the temperature field. This is due to the almost equal diffusion coefficients of heat and mass ($Le \approx 1$). For high gas injection rate the flow field changes dramatically. The fluid moves upward along the walls and the velocity becomes very small. The flow is laminar. The temperature and concentration fields are stratified. At the bottom the gas is almost pure argon and at the top it is almost pure nitrogen. The hot fluid is kept at the bottom by the mass buoyancy, opposing thermal buoyancy. The flow calculated using the Launder and Sharma model is similar to the flow shown in Fig. 6a, only the turbulent viscosity is somewhat lower (max $\nu_T/\nu = 96$).

Depending on the gas injection rate the thermal or mass buoyancy dominates. In Fig. 8 the velocity fields for different gas injection rates calculated with the standard k–ε model are shown. Increasing the gas injection rate from zero the flow has the temperature driven pattern. For injection rates higher than 0.02 mole/m^2/s the flow is no longer steady but becomes periodic with a period of approximately 20 s. The time dependent behaviour of the flow will be discussed later. For gas injection rates higher than 0.07 mole/m^2/s the flow field changes to the concentration-dominated pattern. If the injection rate is decreased subsequently this pattern persists down to an injection rate of 0.03 mole/m^2/s. This means that two solutions of the flow exist for a range of injection rates. For the calculations with the Launder and Sharma model similar behaviour is found. The transition from temperature-dominated to concentration-dominated flow for increasing gas injection occurs at a lower gas injection rate, namely $N = 0.05$ mole/m^2/s. The transition for decreasing gas injection occurs again at 0.03 mole/m^2/s.

In the experiments this hysteretic behaviour was also found. Using smoke visualization the concentration dominated flow could easily be discriminated from temperature-dominated flow (Fig. 7). In the temperature-dominated case (Fig. 7a) the flow is upward in the centre and downwards at the side walls. Furthermore the turbulent eddies are clearly visible. In the concentration-dominated case (Fig. 7b) a layered structure is observed and the flow velocities are very low. If the gas injection rate was increased slowly the temperature-dominated flows could be maintained up to an injection rate of 0.035 mole/m^2/s. Then the concentration-dominated flow is observed. If the gas injection rate was decreased subsequently the concentration-dominated flow was observed until the injection rate was less than 0.015 mole/m^2/s.

The calculated time-averaged velocity profile at $y/H = 0.37$ is shown in Fig. 9. The velocity maxima decrease when the gas injection rate is increased from 0.01–0.04 mole/m^2/s, indicating the damping effect of

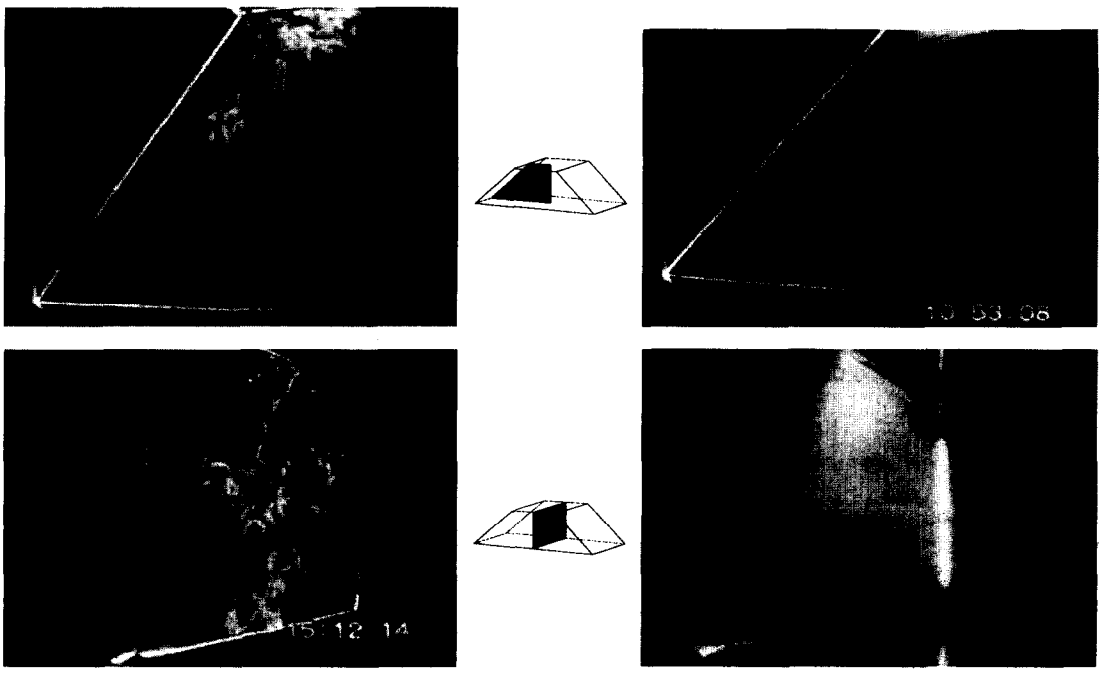

(a) $N = 0.01$ mole/m^{2}s (b) $N = 0.03$ mole/m^{2}s

Fig. 7. Smoke visualization of the flow for low and high gas injection rate, showing the temperature- and concentration-dominated flow pattern. The upper picture is a cross-section in the x–y plane, the lower picture is a cross-section in the y–z plane.

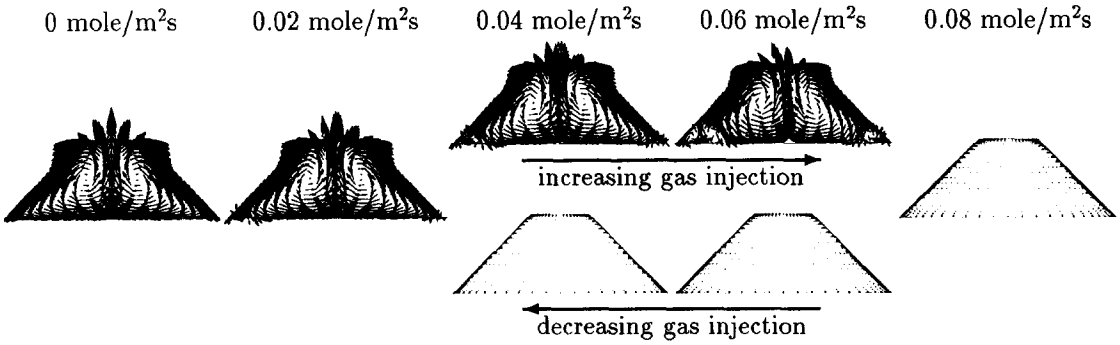

Fig. 8. Velocity field for increasing and decreasing gas injection rate, showing hysteresis.

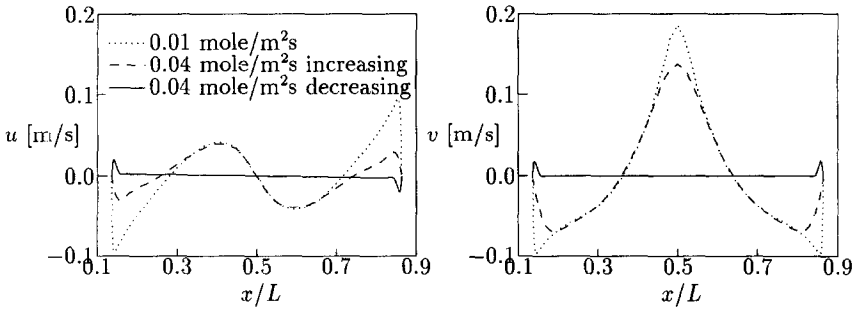

Fig. 9. Horizontal (u) and vertical (v) velocity profiles at $y/H = 0.37$ for different gas injection rates N calculated using the Launder and Sharma model.

the concentration on the thermal buoyancy. The velocity profile for the same gas injection rate ($N = 0.04$ mole/m^2/s), but now in the concentration-dominated state shows that the velocity is much lower now. Only along the side walls there is some flow. This is the injected nitrogen, which moves up past the argon layer.

The turbulent kinetic energy profile is shown in Fig. 10. The turbulence decreases with increasing gas injection rate. In the concentration-dominated flow the flow is laminar and the turbulent kinetic energy vanishes.

Vertical profiles of temperature and concentration at half the cavity length for both temperature-dominated state (increasing N) and concentration-dominated state (decreasing N) are shown in Fig. 11. The profiles calculated using the Launder and Sharma model at $N = 0.04$ mole/m^2/s are compared with measurements at $N = 0.03$ mole/m^2/s. These gas injection rates are not chosen to be the same for this comparison because the region in which the hysteretic behaviour was found was not exactly the same in experiments and simulations. In the temperature-dominated flow regime the temperature and concentration are fairly uniform both in the calculations and in the measurements. Large gradients exist only at the bottom wall. The turbulent flow provides for a high mixing rate in the centre of the trapezoid. In the concentration-dominated regime the calculated vertical temperature and concentration profile show a smooth fall off from pure argon at the hot wall temperature to almost pure nitrogen at the cold wall temperature. Since the flow is laminar the mixing rate is much lower and no uniform profiles are found. The measured temperature profile does not show a smooth fall to the cold wall temperature. The temperature first decreased with increasing height in the cavity, but near the top wall the temperature rises. The top wall is assumed to be adiabatic in the calculations, this means that the temperature of the top wall can change instantaneously when the transition from temperature-dominated to concentration-dominated flow occurs. In the measurements this is of course not possible due

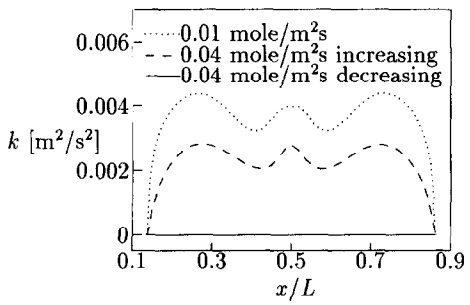

Fig. 10. Turbulent kinetic energy profiles at $y/H = 0.37$ for different gas injection rates N calculated using the Launder and Sharma model.

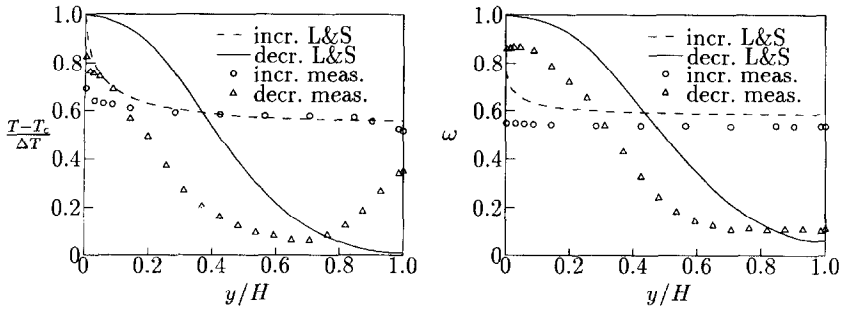

Fig. 11. Temperature and concentration profiles at $x/L = 0.5$ in the temperature-dominated state and the concentration-dominated state. Lines are calculated using the Launder and Sharma model with increasing and decreasing gas injection rate at $N = 0.04$ mole/m^2/s, symbols are measurements for increasing and decreasing gas injection rate at $N = 0.03$ mole/m^2/s.

to the heat capacity of the top wall. Therefore we see that the temperature rises near the top wall. The measured concentration profile shows a smooth curve from $\omega = 0.8$ to $\omega = 0.1$. The shape of the profile is in agreement with the calculations. However, the measured argon concentration is lower. At the bottom wall the gas is not pure argon but a fair amount of nitrogen is present. This is probably due to natural convection flow in the z-direction, which transports nitrogen from the top of the cavity via the relatively cold front and back wall to the bottom.

The average Nusselt number for different injection rates is shown in Fig. 12. The three lines depict the calculations using the standard k–ε model and the Launder and Sharma model in the temperature dominated regime and the laminar calculations in the concentration dominated regime, where no turbulence model is needed. The Nusselt number is calculated by averaging expression (26) over the wall and over time. The hysteresis is clearly visible here. The Nusselt number increases with increasing gas injection rate in both the concentration- and the temperature-dominated regime for both turbulence models. For the concentration-dominated case the Nusselt number increases due to the increased velocity along the walls.

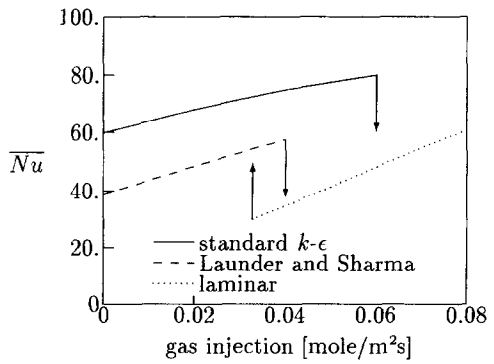

Fig. 12. Average Nusselt number for increasing and decreasing gas injection rate, showing hysteresis.

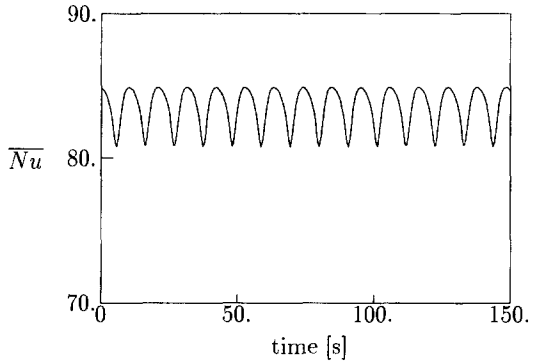

Fig. 13. Streamlines at eight equidistant moments in one period of 21 s for gas injection rate at 0.06 mole/m^2/s.

5.2. *Time dependent behaviour*

The calculations with a non-zero gas injection rate in the temperature-dominated regime converged to periodic solutions. The symmetric pattern of two cells is no longer stable due to the influence of mass buoyancy. The period of the oscillations increases from 19–21 s for gas injection rate from 0.02–0.06 mole/m^2/s in the standard k–ε model calculations. For the Launder and Sharma model the period ranges from 10–38 s for gas injection rates from 0.01–0.04 mole/m^2/s. The size of the oscillations increases with increasing gas injection, indicating that the flow becomes less stable, until the transition to the concentration dominated flow occurs. In Fig. 13 the time dependent behaviour of the flow with gas injection rate 0.06 mole/m^2/s calculated with the standard k–ε model is shown. The streamlines of the flow at eight equidistant moments in one period are shown. In one period first a small convection cell is formed in the corner next to the main convection cell. This small cell increases in size until a second small cell appears in the corner. The second small cell merges with the main cell and the other small cell disappears. This process proceeds in both of the bottom corners. The size of the small cells increases with increasing gas injection rate. The effect

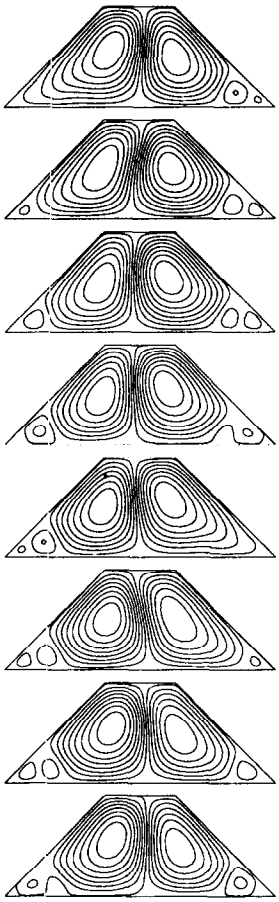

Fig. 14. Time dependent average Nusselt number for gas injection rate of 0.06 mole/m^2/s.

of the periodic flow on the time dependent Nusselt number is shown in Fig. 14.

6. CONCLUSION

From the calculations and measurements of natural convection flow in a trapezoidal cavity the following can be concluded: For temperature driven natural convection the computations of the flow field yielded the predicted velocity field in good agreement with experiments. However, due to three-dimensional effects there is a discrepancy in the central maximum and shape of the vertical velocity profile.

The standard k–ε model and the Launder and Sharma model gave similar velocity fields. The velocity fluctuations and the Nusselt number, however, are significantly different.

In the calculations of the double-diffusive natural convection flow a hysteretic transition from a temperature-dominated to a concentration-dominated regime was observed when the gas injection rate is varied. Both the standard k–ε model and the Launder and Sharma model show this transition, but the gas injection rate where the transition occurs is lower for the Launder and Sharma model.

The existence of the hysteretic transition was confirmed by experiments. The characteristics of the distinctly different flow, temperature and concentration field in the two regimes are in agreement with the calculations.

In the temperature-dominated regime oscillating turbulent flows are found. In the concentration-dominated regime the flow becomes laminar.

Acknowledgement—These investigations are supported by Novem, the Netherlands agency for energy and the environment.

REFERENCES

1. Kuyper, R., van der Meer, T. and Bruining, J., Simulation of underground gasification of thin coal seams. *In Situ*, 1996, **20,** 311–346.
2. Turner, J., The coupled turbulent transport of salt and heat across a sharp density interface. *International Journal of Heat and Mass Transfer*, 1965, **8,** 759–767.
3. Fernando, H., Buoyancy transfer across a diffusive interface. *Journal of Fluid Mechanics*, 1989, **209,** 1–34.
4. Gebhart, B. and Pera, L., The nature of vertical natural convection flows resulting from the combined buoyancy effects of thermal and stress diffusion. *International Journal of Heat and Mass Transfer*, 1971, **14,** 2025–2050.
5. Lin, T. F., Huang, C. C. and Chang, T. S., Transient binary mixture natural convection in square enclosures. *International Journal of Heat and Mass Transfer*, 1990, **33**(2), 287–299.
6. Béghein, C., Haghighat, F. and Allard, F., Numerical study of double-diffusive natural convection in a square cavity. *International Journal of Heat and Mass Transfer*, 1992, **35**(4), 833–836.
7. Nishimura, T., Imoto, T. and Wakamatsu, M., A numerical study of the structure of double-diffusive natural convection in a square cavity. In *Proceedings of ASME/JSME Thermal Engineering Conference*, 1995, **1,** 193–200.
8. Kamakura, K., Double-diffusive natural convection induced by lateral heating and cooling. Ph.D. thesis, Toyama National College of Technology, Toyama, Japan, 1992.
9. Bergman, T., Incropera, F. and Viskanta, R., A differential model for salt-stratified, double-diffusive systems heated from below. *International Journal of Heat and Mass Transfer*, 1985, **28,** 779–788.
10. Bergman, T., Incropera, F. and Viskanta, R., Correlation of mixed layer growth in a double-diffusive, salt-stratified system heated from below. *Journal of Heat Transfer*, 1986, **108,** 206–211.
11. Hanjalić, K. and Musemić, R., Modelling the dynamics of double-diffusive scalar fields at various stability conditions. *International Journal of Heat and Fluid Flow*, 1997, **18,** 360–367.
12. Kuyper, R., Transport phenomena in underground coal gasification channels. Ph.D. thesis, Delft University of Technology, Delft, The Netherlands, 1994.
13. Hanjalić, K., Advanced turbulence closure models: a view of current status and future prospects. *International Journal of Fluid Flow*, 1994, **15,** 178–203.
14. Dol, K. H. H. and Kenjeres, S., A comparative assessment of the second-moment differential and algebraic models in turbulent natural convection. *International Journal of Heat and Fluid Flow*, 1996, **18,** 4–14.
15. Henkes, R., Natural-convection boundary layers. Ph.D.

thesis, Delft University of Technology, Delft, The Netherlands, 1990.
16. Jones, W. and Launder, B., The prediction of laminarization with a two-equation model of turbulence. *International Journal of Heat and Mass Transfer*, 1972, **15,** 301–314.
17. Launder, B. and Sharma, B., Application of the energy-dissipation model of turbulence to the calculation of flow near a spinning disc. *Letters in Heat and Mass Transfer*, 1974, **1,** 131–138.
18. Kuyper, R. and Hoogendoorn, C., Laminar natural convection flow in trapezoidal enclosures. *Numerical Heat Transfer*, 1995, **28,** 55–67.
19. Patankar, S. V., *Numerical Heat Transfer and Fluid Flow*. Hemisphere Publishing Corporation, 1980.
20. Tennekes, H. and Lumley, J., *A First Course in Turbulence*. MIT Press, 1972.
21. Biezen, E., Modelling underground coal gasification. Ph.D. thesis, Delft University of Technology, Delft, The Netherlands, 1996.